PASJ: Publ. Astron. Soc. Japan **60**, 667–681, 2008 August 25

Toward First-Principle Simulations of Galaxy Formation: I. How Should We Choose Star-Formation Criteria in High-Resolution Simulations of Disk Galaxies?

Takayuki R. SAITOH,[1] Hiroshi DAISAKA,[2] Eiichiro KOKUBO,[1,3,4] Junichiro MAKINO,[1,3,4] Takashi OKAMOTO,[5] Kohji TOMISAKA,[1,3,4] Keiichi WADA,[1,3,4] and Naoki YOSHIDA[6]

[1]*Center for Computational Astrophysics, National Astronomical Observatory of Japan, 2-21-1 Osawa, Mitaka, Tokyo 181-8588*
[2]*Graduate School of Commerce and Management, Hitotsubashi University, Naka 2-1 Kunitachi, Tokyo 186-8601*
[3]*Division of Theoretical Astronomy, National Astronomical Observatory of Japan, 2-21-1 Osawa, Mitaka, Tokyo 181-8588*
[4]*School of Physical Sciences, Graduate University of Advanced Study (SOKENDAI), 2-21-1 Osawa, Mitaka, Tokyo 181-8588*
[5]*Institute for Computational Cosmology, Department of Physics, Durham University, South Road, Durham, DH1 3LE, UK*
[6]*Department of Physics, Nagoya University, Furocho, Chikusa, Nagoya 464-8602*
saitoh.takayuki@nao.ac.jp, saitoh.takayuki@cfca.jp

(Received 2007 December 4; accepted 2008 February 18)

Abstract

We performed three-dimensional N-body/SPH simulations to study how mass resolution and other model parameters, such as the star-formation efficiency parameter, C_* and the threshold density for star formation, $n_{\rm th}$ affect structures of the galactic gaseous/stellar disk. We employed 10^6–10^7 particles to resolve a cold ($T < 100\,$K) and dense ($n_{\rm H} > 100\,{\rm cm}^{-3}$) phase as well as diffuse, hot phases. We found that structures of the interstellar medium (ISM) and the distribution of young stars were sensitive to the assumed values of $n_{\rm th}$. High-$n_{\rm th}$ models with $n_{\rm th} = 100\,{\rm cm}^{-3}$ yielded clumpy multi-phase features in the ISM. Young stars were distributed in a thin disk, of which the half-mass scale height was 10–30 pc. In low-$n_{\rm th}$ models with $n_{\rm th} = 0.1\,{\rm cm}^{-3}$, which is usually employed in cosmological galaxy-formation simulations, the gas disk appears to be smoother and the stellar disk is found to be several-times thicker than the high-$n_{\rm th}$ models. A high-resolution simulation with high-$n_{\rm th}$ is necessary to reproduce the complex structure of the gas disk. The global star-formation properties of galaxies, such as the star-formation history, in low-$n_{\rm th}$ models are similar to those in high-$n_{\rm th}$ models when we tune the value of C_* so that they reproduce the observed relation between the surface gas density and the surface star-formation rate density. We however emphasize that high-$n_{\rm th}$ models automatically reproduce the relation, regardless of the values of C_*. The ISM structure, phase distribution and distributions of young star-forming regions are quite similar in runs with different values of C_*. We found that the timescale of the flow from the reservoir ($n_{\rm H} \sim 1\,{\rm cm}^{-3}$) to the star-forming regions ($n_{\rm H} \gtrsim 100\,{\rm cm}^{-3}$) is about five-times as long as the local dynamical time, and this evolution timescale is independent of the value of C_*. The use of a high-$n_{\rm th}$ criterion for star formation in high-resolution simulations makes numerical models fairy insensitive to the modeling of star formation.

Key words: galaxy: evolution — galaxy: ISM — ISM: structure — method: simulation

1. Introduction

A number of physical processes affect the formation and evolution of galaxies. Star formation is among the most important processes, not only because it largely determines the bulk properties of a galaxy, but also because the history of star-formation essentially reflects the formation history of a galaxy.

Numerical simulation is a powerful tool to study galaxy formation. To compare "simulated" galaxies with observed ones, it is necessary to follow the dynamics of baryonic matter as well as the assembly of dark-matter halos. Simulations of galaxy formation are, however, often hampered by the fact that relevant physics are still poorly understood. Numerical resolution is another limiting factor. In particular, appropriate physical models of star formation should be used in high-resolution simulations. For example, recent simulations of galaxy formation (e.g., Governato et al. 2007), have a spatial resolution of several hundreds of pc, with a corresponding mass resolution of $\sim 10^5 M_\odot$. In such simulations, simple models, such as an isothermal interstellar medium (ISM), are applied to galactic gas disks. In addition, individual giant molecular clouds (hereafter GMCs) in galaxies are not resolved in current simulations, although GMCs are regarded as the site of star formation. Thus, one often needs to use phenomenological models, to describe the star-formation processes, which is called subgrid physics.

There are many prescriptions ("subgrid models") of star formation used in simulations of galaxy formation with coarse resolutions. A commonly used technique is to convert high-density gas elements to collisionless "star" particles (e.g., Katz 1992; Navarro & White 1993; Steinmetz & Müller 1994; Mihos & Hernquist 1994; Katz et al. 1996; Yepes et al. 1997; Thacker & Couchman 2001; Abadi et al. 2003; Kawata & Gibson 2003; Sommer-Larsen et al. 2003; Springel & Hernquist 2003; Robertson et al. 2004; Saitoh & Wada 2004; Okamoto et al. 2005; Stinson et al. 2006; Governato et al. 2007; Okamoto et al. 2008). Typical criteria to spawn star particles are as follows (e.g., Navarro & White 1993; Katz et al. 1996; Stinson et al. 2006): (1) the physical density is greater than $n_{\rm H} = 0.1\,{\rm cm}^{-3}$, (2) the temperature is lower than $T \simeq 10000\,{\rm K}$, and (3) the velocity field is converging. If these three conditions are satisfied, 'stars' are then formed at a rate following the local Schmidt law. Namely, the local star formation rate (SFR), $d\rho_*/dt$, is assumed to be proportional to the local gas density, $\rho_{\rm gas}$, and inversely proportional to the local dynamical time, $t_{\rm dyn} \sim (G\rho_{\rm gas})^{-1/2}$:

$$\frac{d\rho_*}{dt} = C_* \frac{\rho_{\rm gas}}{t_{\rm dyn}}, \tag{1}$$

where C_* is the dimensionless star-formation efficiency parameter. The value of this parameter is usually calibrated by the global star-formation properties, the Schmidt–Kennicutt relation (Kennicutt 1998; Martin & Kennicutt 2001). Choosing $C_* \sim 0.01$ reproduces the Schmidt–Kennicutt relation in the local universe (e.g., Navarro & Steinmetz 2000). However, the threshold density is too low, which does not correspond to typical densities of the neutral hydrogen (H I) and molecular hydrogen (H_2) gas in real galaxies.

There are several models that assume higher density regions as star-forming regions. For instance, Kravtsov (2003) adopted $n_{\rm H} > 50\,{\rm cm}^{-3}$ as the star-forming regions in a cosmological simulation of galaxy formation. When he chose a plausible star-formation time, $t_{\rm sf}$: $d\rho_*/dt = \rho_{\rm gas}/t_{\rm sf}$, which is set to a constant ($= 4\,{\rm Gyr}$) in his simulation, the Schmidt–Kennicutt relation is also reproduced. More recently, Tasker and Bryan (2006, 2008) performed adaptive mesh refinement simulations of the ISM in a static halo potential. Their simulations resolve individual star-forming regions (the minimum cell sizes are 25–50 pc). They compared two variants of star-formation criteria: (a) $n_{\rm H} > 10^3\,{\rm cm}^{-3}$, $T < 10^3\,{\rm K}$, and $C_* = 0.5$, and (b) $n_{\rm H} > 0.02\,{\rm cm}^{-3}$, $T < 10^4\,{\rm K}$, and $C_* = 0.05$. Both models also employ converging flows as one of the star-formation criteria and the star-formation law described by equation (1). Interestingly, it is found that both models reproduce the Schmidt–Kennicutt relation. The star-formation histories are also found to be similar. Therefore, their results appear to imply that the global star-formation properties are not sensitive to the details of star-formation prescriptions.

In this paper, we examine how numerical prescriptions of star formation affect the structure of the ISM, and the global star-formation history (SFH) of a galactic disk. In particular, we focus on the threshold density in star-formation criteria ($n_{\rm th}$) and the star-formation efficiency (C_*). We adopted two values of the density threshold: $0.1\,{\rm cm}^{-3}$ (low-$n_{\rm th}$ model) and $100\,{\rm cm}^{-3}$ (high-$n_{\rm th}$ model). We also tested the effect of the star-formation efficiency parameter, C_*, in high-$n_{\rm th}$ models. We performed high-resolution smoothed particle hydrodynamics (SPH) simulations (number of SPH particles are 10^6–10^7) in a galactic potential, and compared the structure of the ISM and stellar disks. We showed that, while both models can exhibit similar SFHs and the relation of surface gas density to surface SFR, only high-$n_{\rm th}$ models have the complex, inhomogeneous, and multiphase ISM. The ISM has a log-normal like probability density distribution (PDF), while a model that does not include either star formation and supernova (SN) feedback has a power-law like PDF; star formation and SN feedback distort PDF. Interestingly, the structure of the ISM, stellar disks, and SFRs (SFHs) are not simply proportional to C_* in high-$n_{\rm th}$ models. This is because the mass-supply timescale from the reservoir ($n_{\rm H} \sim 1\,{\rm cm}^{-3}$) to the star-forming regions ($n_{\rm H} \gtrsim 100\,{\rm cm}^{-3}$) is $\sim 5\,t_{\rm dyn}(n_{\rm H})$, and this timescale is not affected by the adopted value of C_*.

The plan of this paper is as follows. We mention the relation between numerical resolution and the expressible phase of the ISM in section 2. In section 3, we describe the properties of a model galaxy and our numerical methods. Our results are presented in section 4. A summary and discussions are given in section 5.

2. Estimate of Required Resolutions to Appropriately Model the Star Formation

We consider regions with the density being greater than $100\,{\rm cm}^{-3}$ as "star-forming regions". From the Jeans condition, we can estimate the resolution necessary to express the gravitational collapse for a fluid with a given density and temperature. In SPH simulations, this condition is expressed as $M_{\rm Jeans} \gtrsim N_{\rm nb} \times m_{\rm SPH}$, where $M_{\rm Jeans}$ is the Jeans mass, $N_{\rm nb}$ is a typical number of neighbor particles, and $m_{\rm SPH}$ is the mass of an SPH particle (Bate & Burkert 1997; Bate et al. 2003; Hubber et al. 2006). The Jeans condition then determines resolved regions in phase (ρ–T) plane.

Figure 1a shows the limits for several different particle masses. We can accurately treat the gravitational fragmentation of fluid in the upper region of each line in the phase diagram. The line is given in equation (3) in Saitoh et al. (2006). The curve indicates the thermal balance between the cooling and heating that are both adopted in this paper (see section 3). We assume $N_{\rm nb} = 32$. It is clear that a much higher resolution is required in order to resolve the gravitational collapse to dense clouds, e.g., GMCs.

Figure 1b illustrates $M_{\rm Jeans}$ and $m_{\rm SPH}$ for a given critical density, $n_{\rm crit}$, where $n_{\rm crit}$ is defined as values of the density $n_{\rm crit}$ at intersection between the equilibrium ρ–T relation in figure 1a and a constant $M_{\rm Jeans}$ line. The solid curve indicates that $M_{\rm Jeans}$ is a function of $n_{\rm crit}$, while the dashed curve represents $m_{\rm SPH}$ as a function of $n_{\rm crit}$. The red region overplotted on the dashed curve represents $n_{\rm crit}$ of simulations in this paper, where the mass range of SPH particles in simulations is on the order of $10^{2-3}\,M_\odot$ (see table 2). For a comparison, we chose several simulations of galaxy formation [$m_{\rm SPH} \sim 10^6\,M_\odot$ in Abadi et al. (2003); $m_{\rm SPH} \sim 10^5\,M_\odot$ in Governato et al. (2007)] and plotted the corresponding range of the critical density as the blue region.

3. Methods and Models

We investigated the 3-D evolution of a gas disk in a static disk-halo potential. We assumed a Navarro–Frenk–White (NFW) density profile (Navarro et al. 1997) for a dark-matter halo, and a Miyamoto–Nagai model (Miyamoto & Nagai 1975) for a stellar disk. For the halo model, we adopted a cosmological model of a standard cold dark matter (ΛCDM) universe (Spergel et al. 2003). The cosmological parameters are

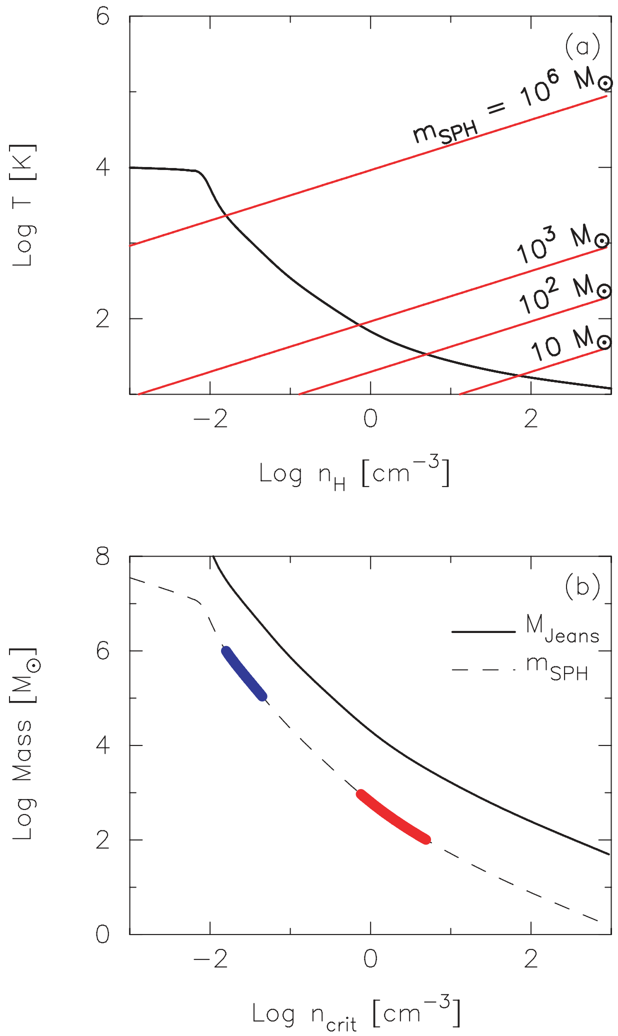

Fig. 1. Required mass resolutions to resolve cold and dense gas phase (a) and the critical density as a function of the Jeans mass in fixed cooling and heating rates used in our simulations (b). The red lines in panel (a) indicate the Jeans limits (the definition is shown in the text) with $m_{\rm SPH} = 10^6$, 10^3, 10^2, and $10 M_\odot$ (from top to bottom), where $m_{\rm SPH}$ is the mass of an SPH particle, and we assume that the Jeans mass is $32 \times m_{\rm SPH}$. The black curve represents the equilibrium temperature of the ISM for the adopted cooling and heating with the solar abundance, $T_{\rm eq}$. For details of the cooling and heating rates, see in subsection 3.1. Panel (b) shows the critical density, $n_{\rm crit}$, where $n_{\rm crit}$ is defined as the values of the density at the intersection between the equilibrium ρ–T relation in panel (a) and the constant $M_{\rm Jeans}$ line, as a function of mass. The thick solid curve shows the $n_{\rm crit}$–$M_{\rm Jeans}$ relation, and the thin dashed curve represents the $n_{\rm crit}$–$m_{\rm SPH}$ relation. We assume that the mass of each SPH particle is the same. The red region overplotted on the dashed curve represents $n_{\rm crit}$ of simulations with $m_{\rm SPH} = 10^{2-3} M_\odot$ (this study), while the blue regions overplotted on the solid curve represents the mass ranges of several simulations of galaxy formation ($m_{\rm SPH} \sim 10^6 M_\odot$ in Abadi et al. 2003; $m_{\rm SPH} \sim 10^5 M_\odot$ in Governato et al. 2007).

$\Omega_{\rm M} = 0.3$, $\Omega_\Lambda = 0.7$, and $H_0 = 70\,{\rm km\,s^{-1}\,Mpc^{-1}}$. We used these parameters to model the dark-matter halo. By adopting static potentials for a dark-matter halo and a stellar disk, we could prevent global disk instabilities and artificial disk heating due to the scattering of gas and star particles by massive dark-matter particles, which are inevitable if we use a live halo with low mass resolution. We will discuss the effect of live halo and also the effect of the mass resolution of halo particles in forthcoming papers.

Gravitational forces were computed by a parallel tree code ASURA (Saitoh, in preparation) that utilize the special-purpose hardware GRAPE. Parallel implementation with GRAPE is based on that of Makino (2004). We used an opening angle $\theta = 0.5$ for a cell opening criterion. We only used a monopole moment. Hydrodynamics was followed by the standard SPH method (e.g., Lucy 1977; Gingold & Monaghan 1977; Monaghan & Lattanzio 1985; Monaghan 1992). The kernel size of each SPH particle was determined by imposing the number of neighbors to be 32 ± 2. We used a cooling function for a gas with the solar metallicity for a temperature from 10 K to 10^8 K (Spaans & Norman 1997). Uniform heating from the far-ultraviolet (FUV) radiation observed in the solar neighborhood (Wolfire et al. 1995) was included. We did not include heating from an ultra-violet (UV) background radiation. This is because we consider the structure of the ISM in the current environment of the Milky Way galaxy in this paper. When we consider the detailed structure of the ISM in the galaxy-formation process, a careful treatment of the UV background and the local FUV radiations is required, since the fluxes are much stronger than those in the local universe in high-redshift universe. This is beyond the scope of this paper.

3.1. Halo+Disk Galaxy Model

We assume that the dark-matter density profile is described by a NFW profile:

$$\rho_{\rm halo}(x) = \frac{\rho_{\rm c}}{x(1+x)^2}, x = r/r_{\rm s}, \tag{2}$$

$$c_{\rm NFW} = r_{\rm vir}/r_{\rm s}, \tag{3}$$

$$M_{\rm vir} = \frac{4\pi}{3}\rho_{\rm cr}\Omega_{\rm M}\Delta_{\rm vir} r_{\rm vir}^3, \tag{4}$$

where $\rho_{\rm c}$ is the characteristic density of the profile, r is a distance from the center of the halo, $r_{\rm s}$ is a scale radius for the profile, $\rho_{\rm cr}$ is the critical density of the universe, and $\Delta_{\rm vir}$ is the virial overdensity (we employ $\Delta_{\rm vir} \equiv 340$). The halo mass is set to be $M_{\rm vir} = 10^{12} M_\odot$ and the concentration parameter is set to be $c_{\rm NFW} = 12$ (Klypin et al. 2002). Then, the profile has $r_{\rm vir} = 258\,{\rm kpc}$, $r_{\rm s} = 21.5\,{\rm kpc}$, and $\rho_{\rm c} = 4.87 \times 10^6 M_\odot\,{\rm kpc}^{-3}$.

The stellar disk is assumed to follow the Miyamoto–Nagai model:

$$\rho_*(R,z) = \left(\frac{M_* z_*^2}{4\pi}\right) \times \frac{R_* R^2 + \left(R_* + 3\sqrt{z^2+{z_*}^2}\right)\left(R_* + \sqrt{z^2+{z_*}^2}\right)^2}{\left[R_*^2 + \left(R_* + \sqrt{z^2+{z_*}^2}\right)^2\right]^{5/2}\left(z^2+{z_*}^2\right)^{3/2}}, \tag{5}$$

with mass M_*, radial scale length R_* and vertical scale length z_*, respectively. R and z are the cylindrical galactcentric radius and the height, respectively. Numerical values of model parameters are given in table 1.

Our model of the gaseous disk is similar to that of Stinson et al. (2006). Initially, the disk has a simple exponential surface density profile. The radial scale length of the gas disk, $R_{\rm gas}$, is

Table 1. Parameters of the model galaxy.

DM halo		Stellar disk			Gas disk				
$M_{\rm vir}$*	$c_{\rm NFW}$†	M_*‡	R_*§	z_*‖	$M_{\rm gas}$#	$R_{\rm gas}$**	$R_{\rm trunc}$††	$z_{\rm gas}$‡‡	$T_{\rm init}$§§
$10^{12} M_\odot$	12	$4.0 \times 10^{10} M_\odot$	3.5 kpc	400 pc	$3.5 \times 10^{9} M_\odot$	7 kpc	10.5 kpc	400 pc	10^4 K

* Virial mass of halo ($M_\odot$). † Concentration parameter. ‡ Mass of stellar disk ($M_\odot$). § Scale length of stellar disk (kpc).
‖ Scale height of stellar disk (kpc). # Mass of gas disk ($M_\odot$). ** Scale length of gas disk (kpc). †† Truncation radius of gas disk (kpc).
‡‡ Initial scale height of gas disk (pc). §§ Initial temperature of gas disk (K).

twice as large as the stellar disk, motivated by the observation of Broeils and Rhee (1997). We truncated the gas disk at $R = 1.5\, R_{\rm gas}$. Note that the truncation radius, $R_{\rm trunc} = 10.5$ kpc, is close to the edge of the molecular disk in the Milky Way galaxy (~ 11 kpc: Nakanishi & Sofue 2006). The initial vertical distribution follows a Gaussian distribution with the scale height of the distribution equal to z_* (see table 1). The total gas mass is $3.5 \times 10^9 M_\odot$. Since we initially placed 10^{6-7} particles in each run, each SPH particle had a mass of 350–3500$M_\odot$ (results of convergence tests are shown in subsection 4.4). The gas disk initially rotates with a circular velocity of the model galaxy. The gravitational softening length is set to be 10 pc for the gas particles. The initial gas metallicity is set to be the solar value.

We evolved the disk without radiative cooling for the first 50 Myr, in order to have a relaxed particle distribution. We checked that our choice of the time duration of this initial relaxation phase does not affect the main results.

3.2. *Star-Formation and Supernova Feedback Models*

We adopted a commonly used condition for star formation: (1) $n_{\rm H} > n_{\rm th}$, (2) $T < T_{\rm th}$, and (3) $\nabla \cdot v < 0$, for a star-formation site. We parameterized the star-formation model by two parameters: $n_{\rm th}$ and $T_{\rm th}$. Here we consider two simple models for star formation. One is $n_{\rm th} = 100\,{\rm cm}^{-3}$ and $T_{\rm th} = 5000$ K. This density corresponds to mean densities of GMCs, while this temperature is much higher than the typical temperature of GMCs ($T < 100$ K). Nonetheless, we find that more than ninety-percent of stars in mass are formed from the gas below $T = 100$ K. The disk structures are thus insensitive to the choice of $T_{\rm th}$. We call this model the "high-$n_{\rm th}$ model". The other is $n_{\rm th} = 0.1\,{\rm cm}^{-3}$ and $T_{\rm th} = 15000$ K. We dub this model the "low-$n_{\rm th}$ model". The low-$n_{\rm th}$ model is similar to what was used in previous simulations of galaxy formation (e.g., Navarro & White 1993; Katz et al. 1996; Thacker & Couchman 2001; Okamoto et al. 2005, 2008; Governato et al. 2007).

When an i-th gas particle is eligible to form stars, we computed the probability, $p_{{\rm SF},i}$, of the particle to spawn a new star particle with mass $m_{*,\rm spawn}$ during a time-step width dt as

$$p_{{\rm SF},i} = \frac{m_{{\rm gas},i}}{m_{*,\rm spawn}} \left[1 - \exp\left(-C_* \frac{dt}{t_{{\rm dyn},i}}\right)\right], \quad (6)$$

where $m_{{\rm gas},i}$ is the mass of the gas particle, and $t_{{\rm dyn},i} = (4\pi G \rho_{{\rm gas},i})^{-1/2}$, respectively. If we used $m_{*,\rm spawn} = m_{{\rm gas},i}$, the masses of the gas particles around star forming regions became heavier by receiving mass from evolved stars, and we lost mass resolution. On the other hand, a too small value of $m_{*,\rm spawn}$ is not favored from a dynamical point of view. We thus fixed $m_{*,\rm spawn}$ to one-third of the original gas particle mass as in Okamoto et al. (2003, 2005). When the mass of a gas particle become smaller than $m_{*,\rm spawn}$, we converted the gas particle into a collisionless particle. We considered each stellar particle to be a single stellar population (SSP) having its own age and metallicity. We assumed the Salpeter initial mass function (Salpeter 1955), whose lower and upper mass limits are $0.1 M_\odot$ and $100 M_\odot$, respectively.

We implemented SN feedback in a probabilistic manner, as in Okamoto, Nemmen, and Bower (2008). We assumed that stars to be more massive than $8 M_\odot$ explode as Type II SNe and each Type II SN outputs 10^{51} erg of thermal energy into the ISM around the SN. In this paper, we only consider the effect of Type II SNe as feedback from stellar particles, since the time integration of each run is done only 0.3–1 Gyr and the lifetime of Type Ia SNe progenitor is $\gtrsim$ Gyr. The number of SNe in each SSP is approximated by a single event. The probability of a SSP i having such event of SN explosion during a time interval dt is given by

$$p_{{\rm SNII},i} = \frac{\int_{t_{{\rm SSP},i}}^{t_{{\rm SSP},i}+dt} r_{\rm SNII}(t')dt'}{\int_{t_{{\rm SSP},i}}^{t_8} r_{\rm SNII}(t')dt'}, \quad (7)$$

where $t_{{\rm SSP},i}$ is the age of the SSP, $r_{\rm SNII}$ is the SN II rate for the SSP, and t_8 is the lifetime of a $8 M_\odot$ star. SN energy is smoothly distributed over the surrounding 32 SPH particles. Here we used the SPH kernel as a weighting function for the energy deposition. The specific SN rate was $\simeq 0.0072\,{\rm SN}/M_\odot$ and the typical stellar mass of each stellar particle was $\sim 1000 M_\odot$ in our simulation with 10^6 particles. Thus, each SN event in our simulation corresponded approximately to an association of $\simeq 7$ SNe.

Table 2 gives the model parameters for our runs. We performed a total of seven runs, and labeled them 'A', 'B', 'C', 'D', and 'E' with two additional runs with extra suffixes, such as 3 and 10. The labels indicate the adopted ranges of the radiative cooling function and the star-formation model. Run A represents a standard model, which is often used in cosmological simulations of galaxy formation. This model employs 10^4 K as the minimum temperature, $T_{\rm cut}$. Then, this model does not have the cold phase gas ($T < 1000$ K). In contrast, Run B adopts $T_{\rm cut} = 10$ K and had the cold phase gas. Both Runs C and D adopted a high-density and low-temperature thresholds, whereas these models had different star-formation efficiencies. Runs C and D employed $T_{\rm cut} = 10$ K. The low star-formation efficiency in Run C was motivated by the slow star-formation model of Zuckerman and Evans (1974) and Krumholz and Tan (2007), whereas the high star-formation efficiency in Run D was motivated by observations of star clusters ($C_* \sim 0.1$–0.3) reported by Lada and Lada (2003). Such

Table 2. Parameters of runs.

Model	N^*	$m_{\rm SPH}{}^\dagger$	$\epsilon^\ddagger$	$T_{\rm cut}{}^\S$	$n_{\rm th}{}^\|$	$T_{\rm th}{}^\#$	$C_*{}^{**}$
Run A	10^6	$3500 M_\odot$	10 pc	10000 K	0.1 cm^{-3}	15000 K	0.033
Run B	10^6	$3500 M_\odot$	10 pc	10 K	0.1 cm^{-3}	15000 K	0.033
Run C	10^6	$3500 M_\odot$	10 pc	10 K	100 cm^{-3}	5000 K	0.033
Run C_3	3×10^6	$1170 M_\odot$	10 pc	10 K	100 cm^{-3}	5000 K	0.033
Run C_{10}	10^7	$350 M_\odot$	10 pc	10 K	100 cm^{-3}	5000 K	0.033
Run D	10^6	$3500 M_\odot$	10 pc	10 K	100 cm^{-3}	5000 K	0.5
Run E	10^6	$3500 M_\odot$	10 pc	10 K	N/A	N/A	N/A

* The initial number of SPH particles. † Mass of individual SPH particles ($M_\odot$).
‡ Gravitational softening length (pc). § Cut off temperature of cooling function (K).
$^\|$ Threshold density of star formation (cm^{-3}). $^\#$ Threshold temperature of star formation (K).
** Star-formation efficiency.

a high efficiency was also adopted in recent simulations by Tasker and Bryan (2006, 2008) ($C_* = 0.5$). Runs C_3 and C_{10} differ from Run C in the mass resolution. Run E excluded the star-formation process. We evolved Runs A, B, C, D, and E for 1 Gyr, whereas we terminated Runs C_3 and C_{10} at 0.3 Gyr because of limitations of the computational resources.

4. Results

We present the three-dimensional structure of the ISM and the distribution of young stars in subsection 4.1. The SFHs and the relation between surface gas density and surface SFR density ($\Sigma_{\rm gas}$–$\Sigma_{\rm SFR}$) are shown in subsection 4.2. Phase (ρ–T) diagrams and the density probability distribution functions (PDFs) are shown in subsection 4.3. The results of the convergence tests are reported in subsection 4.4.

4.1. Features of Disks

4.1.1. Structure of gas disks

Figure 2 shows density and temperature snapshots of Runs A, B, C, and D at $t = 0.3$ Gyr. Different values of $T_{\rm cut}$ lead to different density and temperature structures; the models with $T_{\rm cut} = 10$ K show gas disks with complex and inhomogeneous structures (Runs B, C, and D), whereas the model with $T_{\rm cut} = 10000$ K shows a very smooth gas disk (Run A). Different star-formation criteria yield further different density and temperature structures. The high-$n_{\rm th}$ models have more complex and inhomogeneous structures in the ISM (Runs C and D) than that in the low-$n_{\rm th}$ model with $T_{\rm cut} = 10$ K (Run B).

Run A has a smooth density structure because the higher effective pressure ($T_{\rm cut} = 10000$ K) stabilizes the gas disk. In contrast, Run B had cold clumps because of the lower temperature threshold for star formation, $T_{\rm cut} = 10$ K. Similar influences of $T_{\rm cut}$ on the ISM structure are also reported in Saitoh et al. (2006). In Runs A and B, the ISM formed stars at local density peaks before they developed clumpy structures, such as dense filaments, which are found in high-$n_{\rm th}$ models.

Runs C and D had highly inhomogeneous structures compared with Runs A and B. In these runs, numerous cold and dense ($T \leq 1000$ K and $n_{\rm H} > 10$ cm^{-3}) gas clumps were formed because of the high-$n_{\rm th}$. We can see many filaments and clumps of dense gases as well as 'holes' of diffuse gases. The dense filaments and clumps have 3–4 orders of magnitudes larger densities than the holes. Such structures are rapidly formed after turning on radiative cooling, and they are retained throughout the evolution. A close comparison of Runs C and D revealed that the total mass in dense gas clumps was larger in Run C than in Run D. The volume which was filled with dense gas in Run C also appeared to be larger than in Run D. This is partly because the output time for Run D was just after a star-formation peak (see figure 6).

From edge-on views of density snapshots in figure 2, we find that the gas disks with $n_{\rm H} > 1$ cm^{-3} have a thickness of ~ 200 pc for all of the models. In Run A, the disk had a smooth vertical structure. In Runs B, C, and D, the disks appeared to be rather clumpy, similarly to the results of three-dimensional Eulerian simulations for galactic disk (e.g., de Avillez 2000a, b; Tasker & Bryan 2006; Wada & Norman 2007). The dense clumps had a low temperature ($T < 1000$ K) in these runs.

The temperature distributions are shown in the bottom row of figure 2. Again, Run A had a smooth and high-temperature distribution, while Runs B, C, and D had complex structures of cold gas. It is intriguing that cold components with $T < 1000$ K in Runs B, C, and D are not always associated with dense gas layers (see close up views of density and temperature maps from edge-on). Dense gas layers are heated up by hydrodynamic shocks caused by gravity and SNe. As a result, the temperature at a given density can be different from the equilibrium value. This result is similar to those in previous ISM simulations of galactic disks and circumnuclear disks (e.g., Wada & Norman 1999, 2001; Wada & Tomisaka 2005; Tasker & Bryan 2006).

We define a characteristic scale height for each phase as the height that contains half of the mass of the phase at a given radius. We consider two phases, a cold phase ($10\,{\rm K} < T < 100\,{\rm K}$) and a warm phase ($100\,{\rm K} < T < 10000\,{\rm K}$) and call their characteristic scale heights, $z_{\rm cold}$ and $z_{\rm warm}$, respectively. Figure 3 shows $z_{\rm cold}$ (Runs B, C, and D) and $z_{\rm warm}$ (Runs A, B, C, and D) as a function of R at $t = 0.3$ Gyr. Immediately, we find that the typical vertical distribution is clearly separated by the gas temperature and the distribution is not affected by criteria of star formation in our simulations. In Runs B, C, and D, $z_{\rm cold}$ is 20–50 pc, whereas $z_{\rm warm}$ was 60–120 pc. Run D had two local peaks in the profiles: one is shown in the curve of $z_{\rm warm}$ at $R \simeq 5$ kpc and another one is shown in that of $z_{\rm cold}$ at

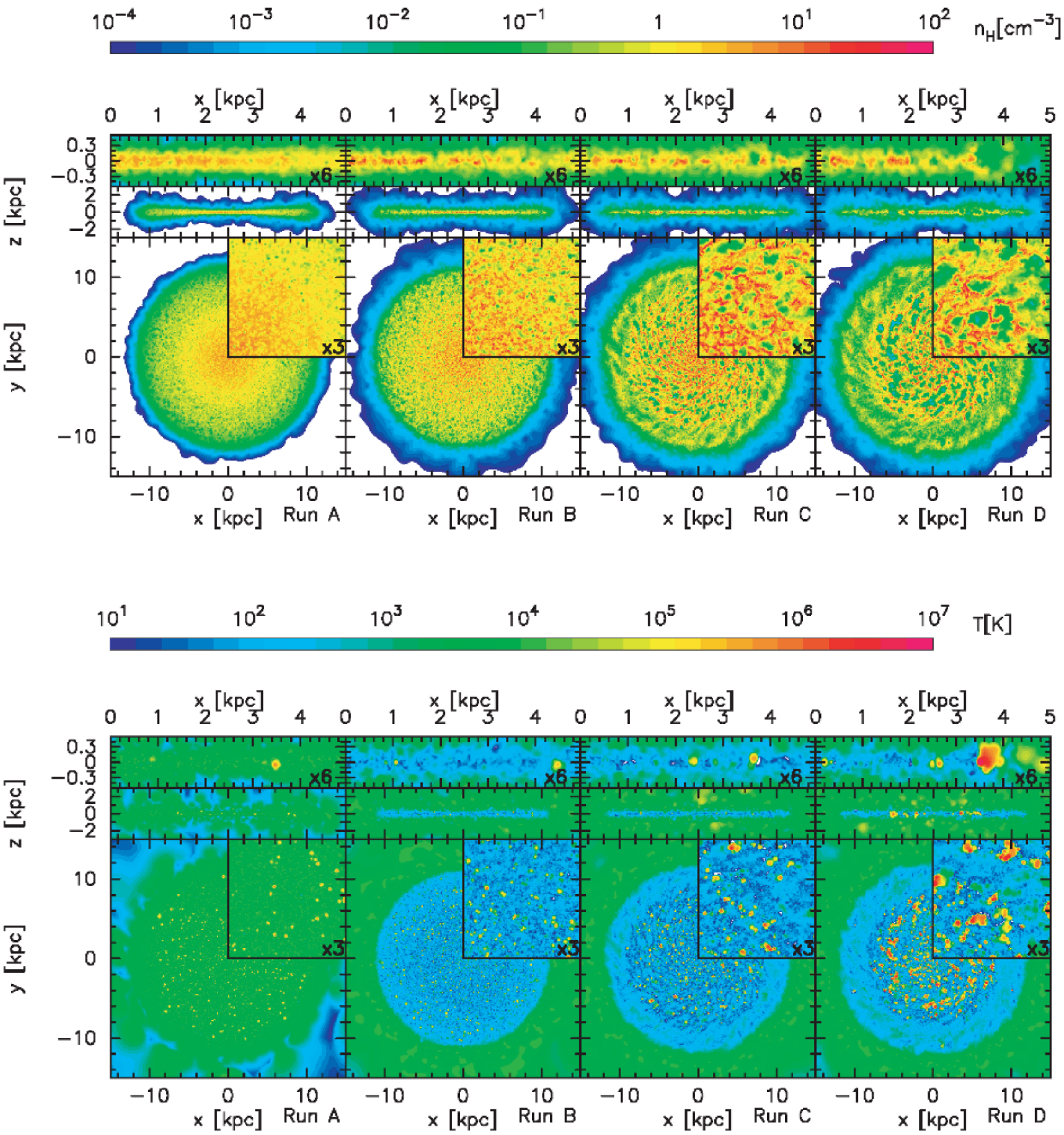

Fig. 2. Density (top row) and temperature (bottom row) snapshots of Runs A, B, C, and D (from left to right), at $t = 0.3\,$Gyr. Top and middle panels show edge-on views (a thin slice of $y = 0$) while the bottom panel shows a face-on view (a thin slice of $z = 0$). The middle panels show a region of $-15 < x < 15\,$kpc and $-2.5\,$kpc $< z < 2.5\,$kpc. The top panels show a region of $0 < x < 5\,$kpc and $-0.42\,$kpc $< z < 0.42\,$kpc. The plot range of the bottom panels is $-15 < x < 15\,$kpc and $-15 < y < 15\,$kpc. The insets in the bottom panels give the close up view of the inner disk for the first quadrant ($0 < x < 5\,$kpc and $0 < y < 5\,$kpc).

$R > 8\,$kpc. These two peaks were induced by the localized SNe and were temporary structures. In Run A, $z_{\rm warm}$ was identical to the others, except at large radii ($R > 7\,$kpc). Hence, the vertical structures of the ISM are basically determined by the ranges of the cooling function. Both $z_{\rm cold}$ and $z_{\rm warm}$ in all runs gradually increased with increasing R. In Run A, the curve of $z_{\rm warm}$ became four-times thicker at the edge than that at center. In Runs B, C, and D, the curves of $z_{\rm cold}$ and $z_{\rm warm}$ became two-times thicker at the edge than those at the centers.

4.1.2. *Structure of stellar disks*

Figure 4 shows face-on and edge-on views of the distribution of star particles for the four runs. We color the figures based on the age of the ten-percent of youngest star particles in each grid as a representative value. The face-on views clearly show that the distributions of stars in Runs C and D had clumpy structures, while Runs A and B had smooth structures. The localization of young stars in high-$n_{\rm th}$ runs can be easily understood by the complex and inhomogeneous structure of the gas disk. A close comparison between figures 2 and 4 reveals that young stars are not always associated with dense gas regions. This is because SN feedback blows out remaining gas around young stars. Consequently, no clear spatial correlation is found between the distributions of young stars and that of dense gas clumps at any given time.

The edge-on views in figure 4 suggest that the vertical distribution of star particles is strongly affected by the threshold density for star formation. This result indicates that $n_{\rm th}$ is an essential parameter that determines the thickness of the stellar disk. We argue that the threshold density needs to be determined by the physical value of the star-forming regions, such as the typical density of molecular clouds.

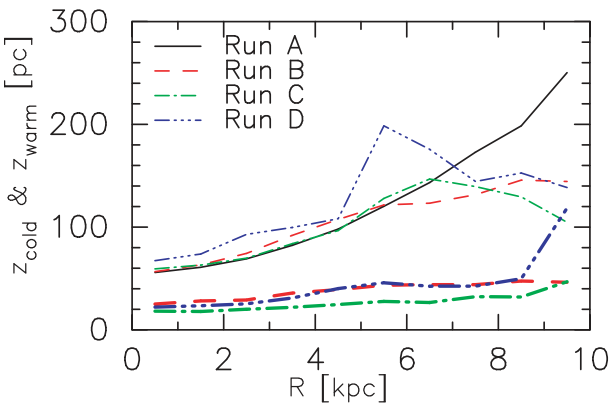

Fig. 3. Half mass heights of gas disks with $T < 100$ K and $100\,{\rm K} < T < 10000$ K at $t = 0.3$ Gyr. The thick curves represent $z_{\rm cold}$, while the thin curves represent $z_{\rm warm}$. Solid (black), dashed (red), dot-dash (green), and dash-dot-dot-dot (blue) curves indicate Runs A, B, C, and D, respectively. The scale of cold gas disk ($z_{\rm cold}$) for Run A is not plotted on this figure.

We further studied the vertical structures of stellar disks. We defined characteristic scale heights as the heights that contain 50%, $z_{*,50}$, and 90%, $z_{*,90}$, of the stellar mass at a given radius. Figure 5 shows $z_{\rm gas,50}$ and $z_{\rm gas,90}$ as a function of R at $t = 0.3$ Gyr. This clearly indicates that the threshold density for the star formation strongly affects the vertical structure of stellar disks. The low-$n_{\rm th}$ models (Runs A and B) have thick, extended stellar disks (30–110 pc for $z_{*,50}$ and 100–300 pc for $z_{*,90}$), whereas the high-$n_{\rm th}$ models (Runs C and D) have very thin stellar disks (10–30 pc for $z_{*,50}$ and 30–60 pc for $z_{*,90}$). We also find that the heights of all stellar disks increase, even weakly, with R. The threshold density has a critical role for stellar disk formation. In contrast, we note that the value of C_* does not significantly affect the vertical structures of stellar disks.

4.1.3. *Disk scale heights: comparison of simulations and observations*

In this subsubsection, we compare the vertical scale heights of three components in our models with observations, namely the vertical distributions of H I and H_2 gas disks, and young star-forming regions (galactic young open clusters). To simplify the comparison, we utilized the half-mass heights in both simulations and observations.

First, we compared $z_{\rm warm}$ with the half-mass height of the galactic H I gas disk, since the typical temperature of H I gas is $100\,{\rm K} < T < 10000$ K (Myers 1978; Spitzer 1978). Nakanishi and Sofue (2003) reconstructed the three-dimensional structure of H I gas of the Milky Way galaxy, by compiling three H I survey data: the Leiden/Dwingelloo survey (Hartmann & Burton 1997), Parkes survey (Kerr et al. 1986), and NRAO survey (Burton & Liszt 1983). They obtained the vertical scale height, which is defined as the full width at half maximum

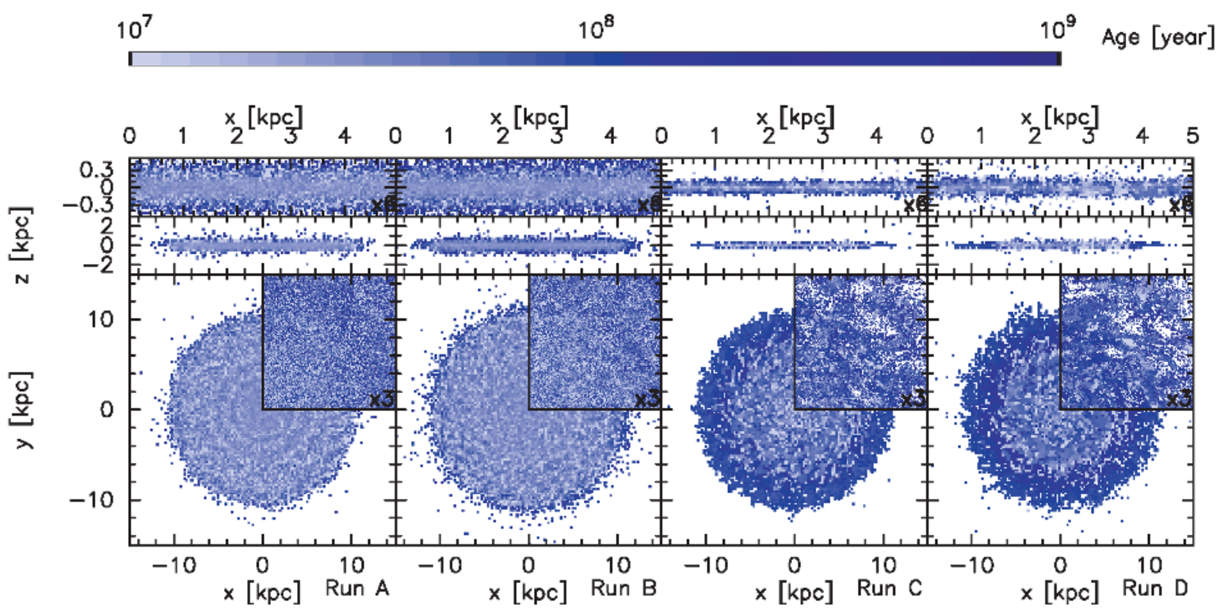

Fig. 4. Projected star particle distributions in face-on and edge-on views of Run A, B, C, and D. Star particles are assigned on uniform grids. Each grid size is 234 pc = (30 kpc/128) for middle and bottom panels, whereas that is 39 pc for top panels and the insets in bottom panels. The color level calculated based on the age of the ten-percent youngest star particles in each grid. The arrangement of the panels is the same as in figure 2.

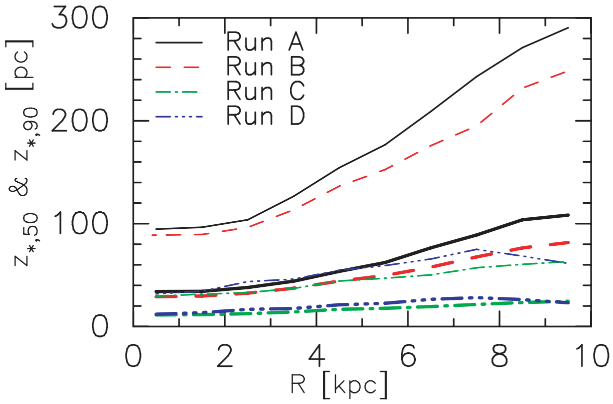

Fig. 5. Half mass and ninety-percent mass heights of stellar disks at $t = 0.3\,$Gyr. The thick curves represent $z_{*,50}$, while the thin curves represent $z_{*,90}$. The solid (black), dashed (red), dot-dash (green), and dash-dot-dot-dot (blue) curves indicate Runs A, B, C, and D, respectively.

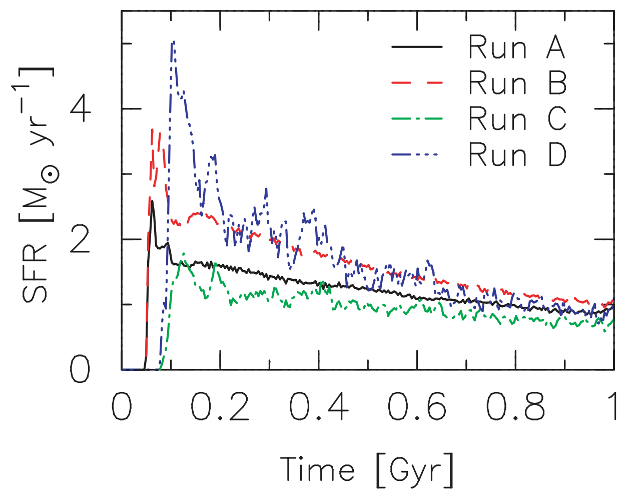

Fig. 6. Star-formation histories in the simulations. The solid, dashed, dot-dash, and dash-dot-dot-dot lines indicate Runs A, B, C, and D, respectively.

(FWHM) as the vertical scale height, as a function of R (see figure 4 in Nakanishi & Sofue 2003). To multiple 0.625 for the FWHM, we obtained the half-mass scale height, since they assumed the vertical distribution of H I gas to be proportional to the square of a function of the hyperbolic secant. The observationally suggested half-mass scale height (60–180 pc at $R = 0$–$10\,$kpc) is almost identical to $z_{\rm warm}$ for the four runs (Runs A, B, C, and D).

Second, we compared $z_{\rm cold}$ and the half-mass scale height of the galactic H_2 gas disk. By using the compilation data of ^{12}CO($J = 1$–0), which is provided by Dame, Hartmann, and Thaddeus (2001), Nakanishi and Sofue (2006) found that the scale heights of the H_2 disk (the FWHM of the H_2 gas disk) in the Milky Way galaxy is 48–160 pc at $R = 0$–$11\,$kpc. Again, we converted the FWHM to the half-mass scale. The half-mass scale of the observed H_2 gas disk is $\sim$ 30–100 pc at $R = 0$–11 kpc. The half-mass scale heights of simulations, $z_{\rm cold}$, are slightly thiner than that in the Milky Way galaxy. However the difference is at most a factor of two. We thus consider that $z_{\rm cold}$ is in good agreement with that in the Milky Way galaxy.

Finally, we compared the vertical scales of star particles with the observed one through mass fractions. The vertical distribution of galactic young open clusters is a good tracer of the recent star-forming regions in the Milky Way galaxy. As shown in Janes and Phelps (1994), the vertical distribution of galactic young clusters of which the ages are shorter than that of Hyades ($\sim$ 800 Myr) is fitted by an exponential function with a 55-pc scale-height. The half-mass height of the exponential profile is $\simeq$ 38 pc (0.69 × 55 pc). Star particles in high-$n_{\rm th}$ models (Runs C and D) have $z_{*,50} \sim$ 10–30 pc, whereas stars in the low-$n_{\rm th}$ models (Runs A and B) are more broadly distributed in the vertical direction, $z_{*,50} \sim$ 60–100 pc. Only the high-$n_{\rm th}$ models are consistent with the observation. It should be noted that even in Run B, which includes cooling under 10^4 K, the scale height is too large. We can conclude that $n_{\rm th}$ is a key parameter to determine the thickness of stellar disks.

4.2. *SFHs and $\Sigma_{\rm gas}$–$\Sigma_{\rm SFR}$ Relations*

Figure 6 compares the global SFHs in four runs (Runs A, B, C, and D). In all runs, the SFHs are characterized by an initial rapid increase, followed by a gradual decrease. The rapid increase continues for only $\sim 10^7$ yr because of SN feedback effects. The evolutions after the first peak are described approximately by an exponential decay with short-period spikes. We find that the SFRs asymptotically decrease to $\sim$ 1–2 $M_\odot\,{\rm yr}^{-1}$, which is close to the observational value of SFR in nearby spiral galaxies ($\sim 1 M_\odot\,{\rm yr}^{-1}$: James et al. 2004) and Galactic SFR ($\sim 3 M_\odot\,{\rm yr}^{-1}$: McKee & Williams 1997).

It is worth pointing out that the difference in the global SFHs of Runs C and D is rather small, despite a factor of 15 ($= 0.5/0.033$) difference in C_*. Tasker and Bryan (2006) performed test simulations by changing C_* by a factor of ten, and found that it has little effect on the global SFHs. In other words, global SFHs are not directly proportional to C_* when a high-density threshold is adopted. They claimed that this is because the dynamical time in star-forming regions is sufficiently shorter than that in galaxies. As discussed in subsubsection 4.3.2, we found that the contraction timescale of the gas is about 5-times longer than the local dynamical time, and that this timescale does not depend on the value of C_*. Hence, the global SFH is not directly proportional to C_*.

Figure 7 presents $\Sigma_{\rm gas}$–$\Sigma_{\rm SFR}$ relations for Runs A, B, C, and D. All of our runs show similar relations, both in the slope and in the normalization, to the observational values (−1.4: solid lines in the figure), although the range covered by our simulations is somewhat limited. Slightly steeper slopes in Runs with a high critical density (i.e., Runs C and D) than Run A are consistent with what Wada and Norman (2007) found in their theoretical model of global star formation in the ISM with log-normal density PDF. We have shown that the different threshold models have very different ISM structures. The distributions of newly formed star particles are also different, reflecting the structures of the ISM. Nevertheless, as we have shown, the observed $\Sigma_{\rm gas}$–$\Sigma_{\rm SFR}$ relation was well reproduced in all of our simulations.

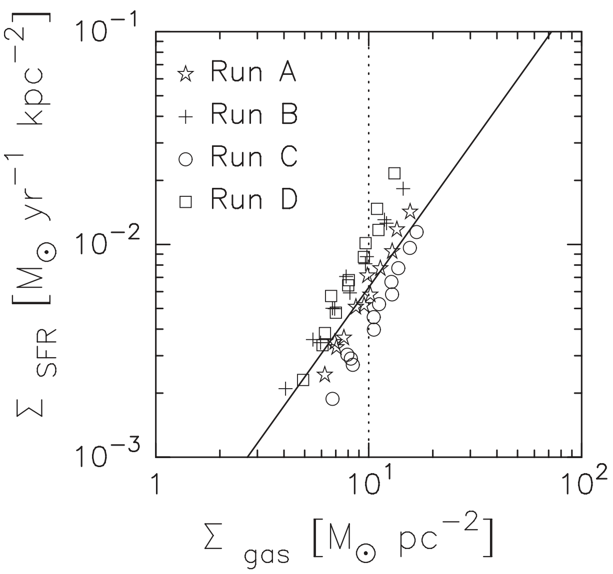

Fig. 7. Surface gas density and the surface star-formation rate for Runs A, B, C, and D in three different epochs $t = 0.3$, 0.5, and 1.0 Gyr. The surface SFRs are computed using the surface densities of young star particles of which ages are shorter than the typical age of massive stars; 4.5×10^7 yr. The outer edges of surface densities correspond with the distance of the most distant young star particle from the galactic center and the typical edges of the star-forming regions are $R \simeq 10$ kpc. Four cylindrically averaged values with a constant radial interval are obtained from each run and each epoch. Stars, crosses, circles, and squares represent the sequences of Runs A, B, C, and D, respectively. The solid line is a best fit from observations (Kennicutt 1998).

4.3. *Phase Structure of the ISM*

In this subsection, we consider the phase structures of the ISM in more detail. The differences between the low-$n_{\rm th}$ and high-$n_{\rm th}$ models in the phase diagram are discussed in subsubsection 4.3.1. The distribution functions of the gas mass as a function of the density and the temperature are also discussed. The evolution of individual gas particles is analyzed in subsubsection 4.3.2. We find from the analysis that the evolution timescale of the ISM ($1\,{\rm cm}^{-3} < n_{\rm H} < 100\,{\rm cm}^{-3}$) is typically $\sim 5\,t_{\rm dyn}(n_{\rm H})$. We show the PDFs of Runs C, D, and E in subsubsection 4.3.3. The high-density parts of PDFs in Runs C and D were well-fitted by a log-normal function, whereas that in Run E was a single power-law like form. In our simulations, the form of PDF changes by the effects of star formation and SN feedback.

4.3.1. *Phase diagram*

In figure 8, we show global phase (ρ–T) diagrams of Runs A, B, and C at $t = 0.3$ Gyr. The phase diagram in Run D resembles that in Run C, and thus we exclude it here. Differences in the phase distribution between Runs C and D are discussed in subsubsection 4.3.3. The phase structures in different runs are very different. Phase structures strongly depend on $n_{\rm th}$ and $T_{\rm cut}$. As a consequence of the assumption ($T_{\rm cut} = 10^4$ K), Run A consists of a warm ($T \sim 10^4$ K) and a hot ($T > 10^5$ K) phase. There is no cold phase because of the cut-off temperature of the cooling function, $T_{\rm cut}$, whereas the hot phase is formed by the SN feedback. In Run A, there is a density cut off at $n_{\rm H} \sim 10\,{\rm cm}^{-3}$ because the star

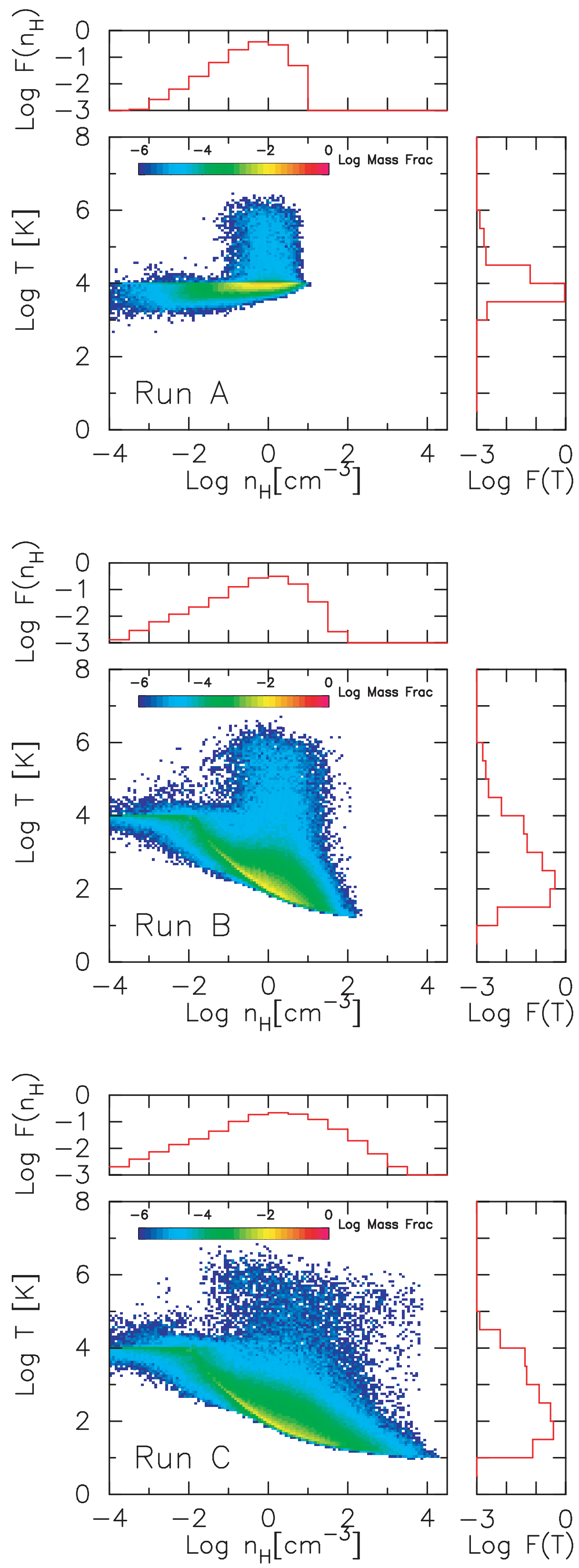

Fig. 8. ρ–T diagram for Runs A, B, and C (from the top panel to the bottom panel). All plot regions are subdivided into 128×128 grids, and each grid is colored by a mass fraction. The top and right histograms in each panel show mass fractions as functions of the density and the temperature.

formation is rapidly consuming high-density gas and the gas pressure with $T = 10^4\,\mathrm{K}$ prevents further collapse. The overall feature is similar to that in Stinson et al. (2006), and the assumption ($T_{\mathrm{cut}} = 10^4\,\mathrm{K}$) is reasonable for coarse resolution ($m_{\mathrm{SPH}} \sim 10^{5-6}\,M_{\odot}$) runs (see figure 1). Runs B and C showed a clear multiphase structure with a cold gas. The high-density gas in Run B became denser than that in Run A due to the low effective pressure. The high-density tail extends to $n_{\mathrm{H}} \sim 100\,\mathrm{cm}^{-3}$ in this case. The high-n_{th} model has more dense and cold gas, since the gas consumption due to star formation occurred at $n_{\mathrm{H}} \sim 100\,\mathrm{cm}^{-3}$. The multiphase structure in Run C was similar to those obtained in previous high-resolution grid-base simulations (e.g., Wada & Norman 1999; Wada 2001; Tasker & Bryan 2006).

The mass fractions as a functions of density $F(n_{\mathrm{H}})$ and temperature $F(T)$ are shown in the top and right histograms in each panel of figure 8. In Run A, the peak of $F(n_{\mathrm{H}})$ is $n_{\mathrm{H}} \sim 1\,\mathrm{cm}^{-3}$ and that of $F(T)$ is $T \sim 10^4\,\mathrm{K}$. The temperature peak shifted to $T \sim 100\,\mathrm{K}$ in Run B. The dominant component in temperature in Run C was also the cold phase gas ($T <$ 1000 K) as was also found in other high-resolution simulations of the ISM, i.e., $\sim$ 80–90% of mass in the ISM was in the cold phase (i.e., Rosen & Bregman 1995; Wada 2001; Tasker & Bryan 2006). The peak of $F(n_{\mathrm{H}})$ is $n_{\mathrm{H}} \sim 1\,\mathrm{cm}^{-3}$ and that of $F(T)$ is $T \sim 100\,\mathrm{K}$. In conclusion, the multiphase ISM in the high-n_{th} models has a large mass of reservoir around $n_{\mathrm{H}} = 1\,\mathrm{cm}^{-3}$ for the star-forming region ($n_{\mathrm{H}} > 100\,\mathrm{cm}^{-3}$). Thus, the evolution of the reservoir should play a key role for star formation in the multiphase ISM. We further consider the evolution of the gas from the reservoir to star-forming regions in the next subsubsection.

4.3.2. *Detailed evolution of fluid elements in the multiphase ISM*

Figure 9 shows the evolution of gas in the phase (ρ–T) diagram within $\Delta t \equiv 1\,\mathrm{Myr}$ at $t = 0.3\,\mathrm{Gyr}$ in Runs A and C. There was a main stream toward higher densities between T_{eq} and $10^{0.5} \times T_{\mathrm{eq}}$ in Run C, while we could not find any flow in that direction in Run A. We computed the mass flux on the phase diagram around the main stream, between T_{eq} and $10 \times T_{\mathrm{eq}}$, toward high density with binning from $\log(n_{\mathrm{H}}) = 0$ to $\log(n_{\mathrm{H}}) = 2$ every $1/3$ dex in density. The median values were adopted for the indicator of the density evolution in each bin. Figure 10 shows the e-folding (evolution) times in Runs C and D. We define the evolution time that the density changes e times by the evolution time of the medians within Δt interval on the phase diagram:

$$t_{\mathrm{evo}} \equiv \rho_{\mathrm{m}}/(\Delta\rho_{\mathrm{m}}/\Delta t), \tag{8}$$

where ρ_{m} are the initial values of the median densities and $\Delta\rho_{\mathrm{m}}$ is the density changes of ρ_{m} within Δt, respectively. We then found that the evolution time is $t_{\mathrm{evo}} \sim 5\,t_{\mathrm{dyn}}(n_{\mathrm{H}})$: $t_{\mathrm{evo}}(n_{\mathrm{H}} \sim 100\,\mathrm{cm}^{-3}) \sim 20\,\mathrm{Myr}$ and $t_{\mathrm{evo}}(n_{\mathrm{H}} \sim 1\,\mathrm{cm}^{-3}) \sim 130\,\mathrm{Myr}$. The analysis on Run D shows almost the same results [compare the thin (Run D) and solid (Run C) lines in figure 10]. Interestingly, the density dependence is proportional to the local dynamical time: $t_{\mathrm{evo}} \propto \rho^{-1/2}$. A comparison between Runs C and D indicates that the evolution timescale in the multiphase ISM is independent of the star-formation efficiency, C_*.

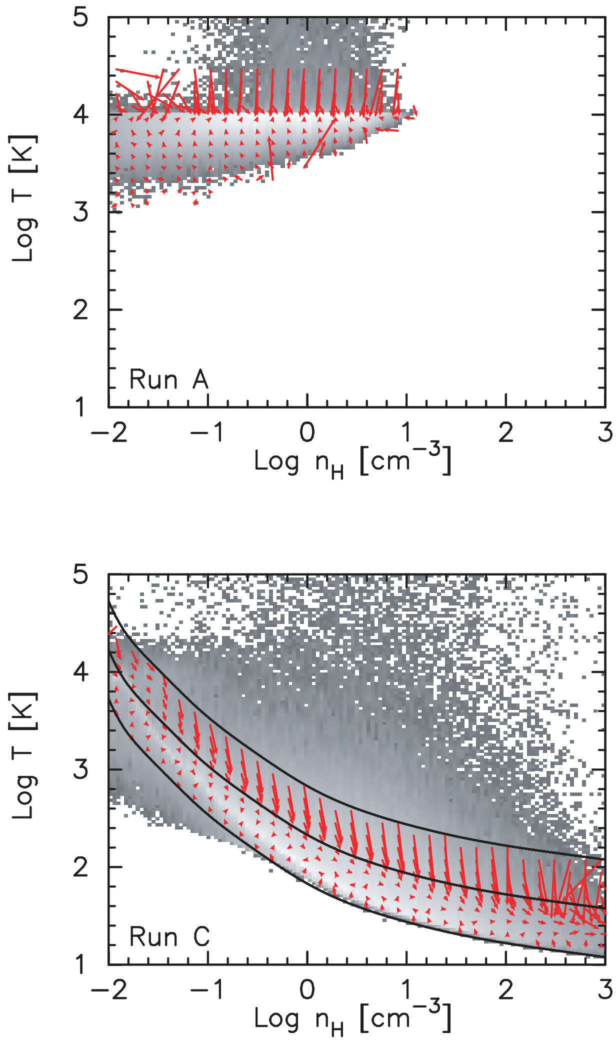

Fig. 9. Evolution of SPH particles in each grid on phase diagram within $\Delta t = 1\,\mathrm{Myr}$ at $t = 0.3\,\mathrm{Gyr}$ in Runs A (top panel) and C (bottom panel). Arrows indicate evolution of sampled grids on the phase diagram in $T < 10^5\,\mathrm{K}$ for Run A and in $T_{\mathrm{eq}} < T < 10 \times T_{\mathrm{eq}}$ for Run C. The heads of arrows indicate the median values of density and temperature after Δt of evolution. Black curves indicate the equilibrium temperature of the adopted cooling and heating with the solar abundance, T_{eq}, and its families that $10^{0.5}\ T_{\mathrm{eq}}$ and $10\ T_{\mathrm{eq}}$, respectively. Background gray scales indicate mass weighted distributions of gas on phase diagram.

Figure 11 shows the density evolutions of several selected SPH particles in Run C. There are five loci of randomly selected SPH particles from 190 Myr to 280 Myr. All of the particles have density changes of $\sim$ 5 orders of magnitude. The evolutions are not monotonic, but complex with many compressions and expansions. The considerable drive mechanisms of the compressions are gravitational collapses and hydrodynamical shocks, whereas those of the expansions are SNe and shear extensions. The global evolution of the ISM is expressed by superpositions of the above mechanisms. Hence, the mass flow from $n_{\mathrm{H}} \sim 1\,\mathrm{cm}^{-3}$ to $\sim 100\,\mathrm{cm}^{-3}$ is decelerated compared with that expected by only gravitational collapse.

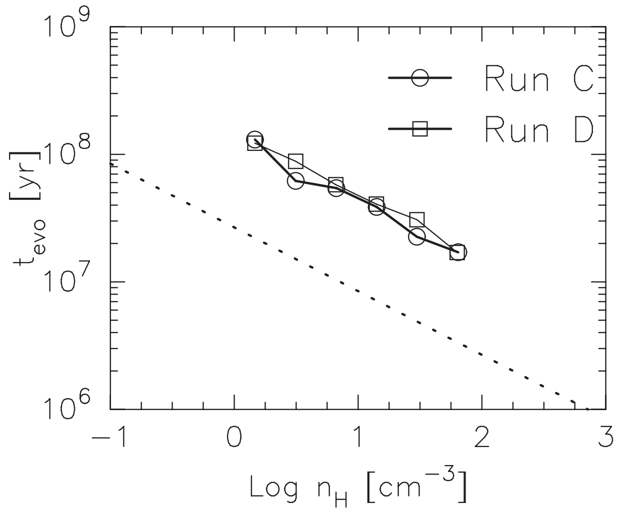

Fig. 10. The e-folding times of density evolution for Run C (the thick solid line with circles) and Run D (the thin solid line with boxes). See the text for the definition of the evolution timescale. Dotted line represents the local dynamical time as a function of the density.

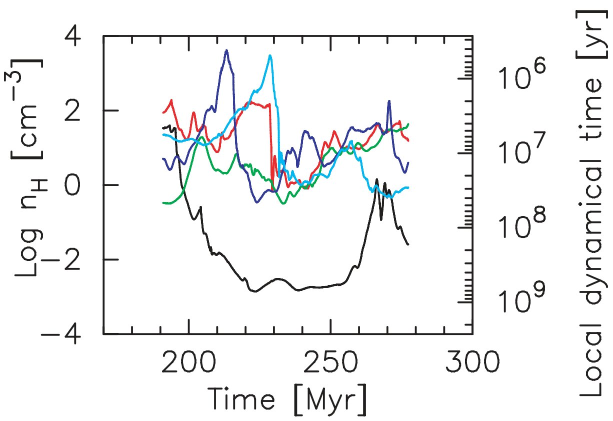

Fig. 11. Evolution tracks of densities for randomly selected SPH particles from 190 Myr to 280 Myr in Run C. The five colors denote five different particles. The corresponding local dynamical time for the density is shown an the right side.

4.3.3. The density PDF

The shapes of the PDF of the ISM give us an idea to connect the global structure of the ISM and star-forming regions. There have been a number of studies on this issue (e.g., Vázquez-Semadeni 1994; Scalo et al. 1998; Vázquez-Semadeni et al. 2000; Wada 2001; de Avillez & Mac Low 2002; Kravtsov 2003; de Avillez & Breitschwerdt 2004; Slyz et al. 2005; Wada & Norman 2007; Tasker & Bryan 2008; Robertson & Kravtsov 2008). When the fluid evolution is dominated by a random density change without any scale dependence, it is expected that the volume-weighted PDF becomes a 'log-normal' distribution (Vázquez-Semadeni 1994). In the multiphase ISM, there are many physical processes, such as radiative cooling, FUV heating, star formation, SN feedback, hydrodynamical shock, and self-gravity. It is unclear whether the combination of these processes is either scale-invariant or not. The expected form of the resultant PDF is also unclear.

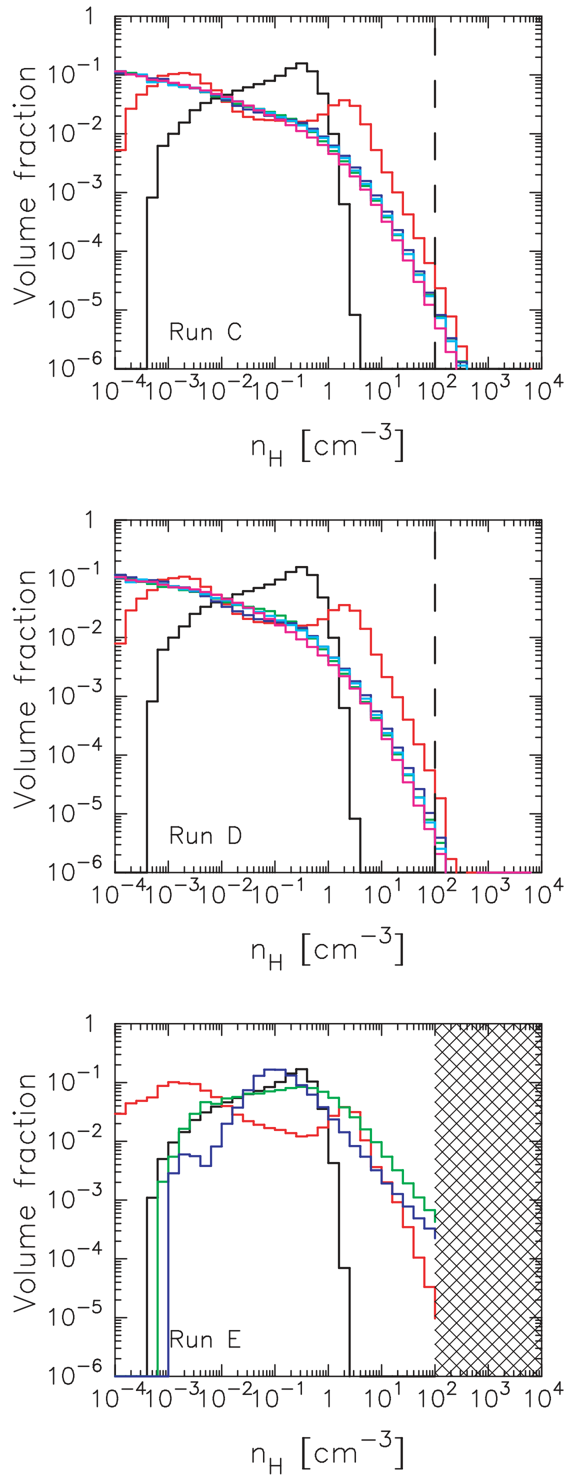

Fig. 12. Volume-weighted probability distribution functions (PDFs) of Runs C, D, and E (from top to bottom) within $R < 10$ kpc. We calculated the volume fraction of an SPH particle by $V_i = m_i/\rho_i$. The density interval was 0.2 dex. The PDFs were normalized to unity. Runs C and D showed six different epochs ($t = 0$, 0.1, 0.2, 0.3, 0.5, and 1.0 Gyr), while Run E showed first four epochs. The black, red, green, blue, sky blue, and magenta indicate PDFs of different epochs $t =$ 0, 0.1, 0.2, 0.3, 0.5, and 1.0 Gyr, respectively. The vertical dotted lines correspond with the star-formation threshold density, $n_{\rm th} = 100\,{\rm cm}^{-3}$. The high-density region ($n_{\rm H} > 100$ cm^{-3}) in Run E is hatched, since the region has artificial mass stagnation due to insufficient mass resolution.

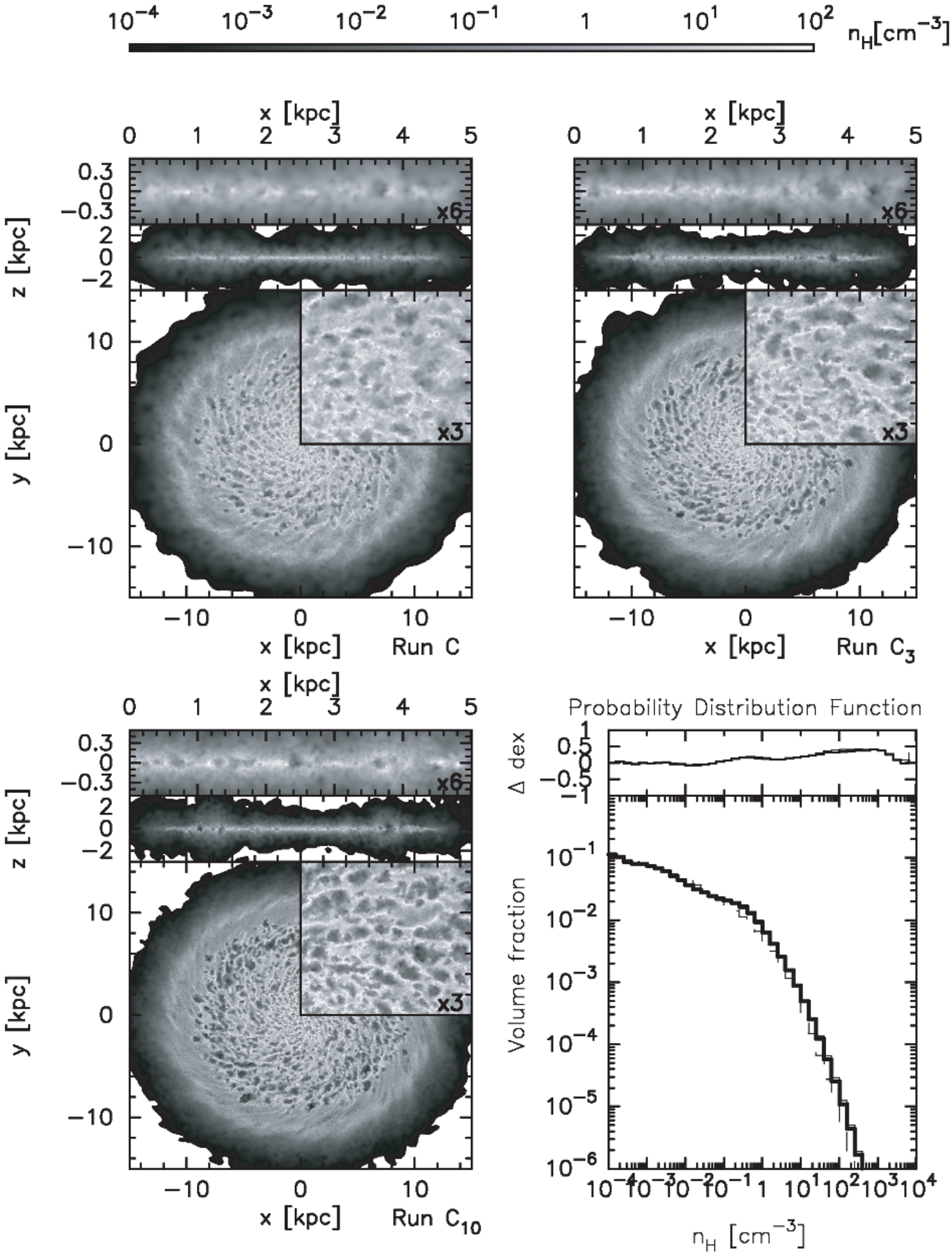

Fig. 13. Sets of panels at the tops and left-bottom are gas-density maps for three different mass resolutions ($N = 10^6, 3 \times 10^6$, and 10^7, respectively). The right-bottom panel shows the PDFs of three runs at $t = 0.3$ Gyr. The thin dashed, thick solid, and thin solid lines indicate simulations using $N = 10^6$, 3×10^6, and 10^7, respectively. PDF residuals of Runs C_3 and C_{10} from C are shown in the upper portion of the panel.

Figure 12 shows the evolutions of PDFs in our SPH simulations. Here, we plot only the PDFs of Runs C, D, and E. The evolutions of the PDFs in these three runs are almost the same that at the first phase, although the quasi-static final shapes depend on the models. At the initial state, the PDFs have uniform density distributions with a peak around $n_{\rm H} \sim 0.3\,{\rm cm}^{-3}$. The PDFs are smoothed out within the first $\sim 0.2\,$Gyr. Our PDFs in the three runs then become quasi-static, as reported by Wada and Norman (2001), Kravtsov (2003), and Wada and Norman (2007). High density tails ($n_{\rm H} > 1\,{\rm cm}^{-3}$) in Runs C and D were in a steady state and had log-normal forms (e.g., Vázquez-Semadeni 1994; Vázquez-Semadeni et al. 2000; Wada 2001; Kravtsov 2003; Wada & Norman 2007; Tasker & Bryan 2008). The high-density tail in Run E (the model did not include either star formation or SN feedback) was asymptotic to a power-law form (green and blue lines). The difference in high-density region came from the fact that the gas in the high-density region converted into stars and SN feedback blew out the surrounding dense gas in Runs C and D. Slyz et al. (2005) showed that a high-density tail of a PDF had a power-law like form in a self-gravity-dominated system, although several authors argued that the log-normal PDF is robust structures of the multiphase ISM, regardless of the input physics (Wada & Norman 2001; Kravtsov 2003). Further investigation into the details is required for the response of the input physics (e.g., UV radiation: Susa & Wada, in preparation) in the form of the PDF.

4.4. *Convergence Tests*

Figure 13 shows density maps in simulations using $N = 10^6$, 3×10^6, and 10^7 (Runs C, C_3, and C_{10}) at $t = 0.3\,$Gyr. At the time, the numbers of particles in all of runs increase by $\sim 30\%$ from the initial states due to star formation. The density distributions indicate that any differences among the three runs with different mass resolutions are very little. These gas disks have almost the same sizes of filaments and voids. The complexness of the gas disks is almost the same degree. The statistical structures of the multiphase ISM, PDFs, in the three runs are also similar to one another (see the lower-right panel in figure 13). Differences are found in the high-density tails from residuals. However, the residuals are only a factor of three at most. Figure 14 shows the vertical thicknesses of stellar disks. These thickness are almost the same for all runs. Thus, we consider that our results are roughly converged in above mass resolutions, for our selected values of $n_{\rm th}$ and $T_{\rm cut}$.

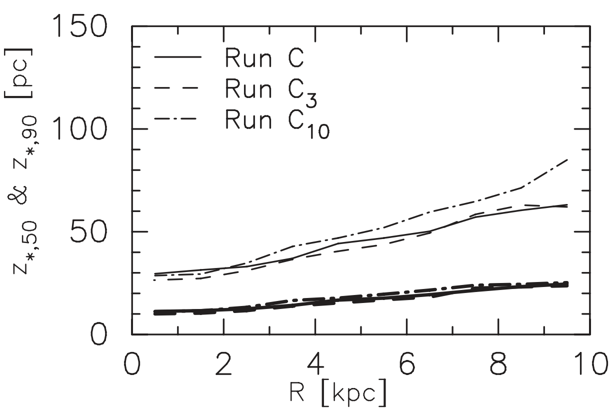

Fig. 14. Same as figure 5, but for Runs C, C_3, and C_{10}.

5. Summary and Discussion

5.1. *Importance of the Density Threshold for Star Formation*

In many studies, numerical models of star formation in galaxy formation have been calibrated to be consistent with the observational $\Sigma_{\rm gas}$–$\Sigma_{\rm SFR}$ relation. For example, Stinson et al. (2006) successfully reproduced the relation with a threshold density of $n_{\rm th} = 0.1\,{\rm cm}^{-3}$. In order to reproduce the relation within simulated disk galaxies, Springel and Hernquist (2003) and Schaye and Dalla Vecchia (2008) explicitly involved the Schmidt–Kennicutt relations in star-formation models in the ISM. Kravtsov (2003) showed that a high-density threshold ($n_{\rm th} = 50\,{\rm cm}^{-3}$) with a constant star-formation time ($= 4\,$Gyr) reproduce the $\Sigma_{\rm gas}$–$\Sigma_{\rm SFR}$ relation. Tasker and Bryan (2006, 2008) reported on a comparison of the low-$n_{\rm th}$ and high-$n_{\rm th}$ star-formation model. Their simulations revealed that both models are able to reproduce the observed $\Sigma_{\rm gas}$–$\Sigma_{\rm SFR}$ relation. We examined two models, a low-$n_{\rm th}$ model ($n_{\rm th} = 0.1\,{\rm cm}^{-3}$; Runs A and B) and a high-$n_{\rm th}$ model ($n_{\rm th} = 100\,{\rm cm}^{-3}$; Runs C and D). Our results also show that both models could reproduce the $\Sigma_{\rm gas}$–$\Sigma_{\rm SFR}$ relation (see figure 7).

We argue that we should generate "stars" above the physical density of real star-forming regions, such as GMCs or molecular cores, to investigate the detailed structure and evolution of disk galaxies. In this paper, we highlighted on the ISM structure and the distribution of newly formed star particles. We found that (1) only the high-$n_{\rm th}$ model reproduces the complex, inhomogeneous, and multiphase ISM structures (see figures 2 and 4), where the cold gas dominates in mass (see figure 8). These natures are very comparable with other studies of the ISM: the geometrically complex and inhomogeneous structures of the ISM (e.g., Rosen & Bregman 1995; Wada & Norman 1999; de Avillez 2000a; de Avillez & Berry 2001; Tasker & Bryan 2006, 2008), three phases structures of the ISM where the cold mass dominates (e.g., McKee & Ostriker 1977; Myers 1978; Rosen & Bregman 1995; Wada 2001; Tasker & Bryan 2006, 2008). The log-normal PDF in the ISM is also found in the high-$n_{\rm th}$ models (see figures 12 and 13), although the origin of the log-normal shape appear to be different from that in previous studies (e.g., Vázquez-Semadeni 1994; Vázquez-Semadeni et al. 2000; Wada 2001; Kravtsov 2003; Wada & Norman 2007; Tasker & Bryan 2008). (2) Only the high-$n_{\rm th}$ models can reproduce observationally reported scale heights of gas disks and young star-forming regions, as shown in figures 3 and 5. Therefore, we emphasize that the density threshold for the star-formation model is the key parameter to model realistic three-dimensional structures of galaxies, especially gas and stellar disk structures. We have to choose the star-forming gases as the physical one for this purpose. It is necessary to solve the energy equation for a much lower temperature gas than $10^4\,$K to resolve the high-density gas. This requires a higher mass resolution than those used in previous simulation of galaxy formation.

5.2. *Weak Dependence on Star Formation Efficiency*

Runs C and D differ in the values of C_*. The results are, however, similar in terms of the ISM structure and stellar disks (figures 2 and 4), the SFHs (figure 6), the $\Sigma_{\rm gas}$–$\Sigma_{\rm SFR}$ relation (figure 7), and the phase distribution of the ISM (figure 12). Why do the simulations show similar results? As shown in figure 8, a large fraction of the gas exists at around $n_{\rm H} \sim 1\,{\rm cm}^{-3}$, and it behaves as a reservoir of the star-forming gas. The mass supply timescale from the reservoir to the star-forming region determines the global star-formation rate in the model that adopts the high-density threshold ($n_{\rm th} = 100\,{\rm cm}^{-3}$). From figure 10, we find that the timescale is $\sim 5\,t_{\rm dyn}(n_{\rm H})$ and the timescale is independent of the values of C_*. Hence, C_* has only weak effects on the global features of the ISM and stellar disks formed from the ISM.

One of the most important advantages of the high-$n_{\rm th}$ model is that the global SFR is not determined by the local quantities, but by the global state of the ISM. The exact value of C_* is unimportant in galactic-scale simulations; hence, we can effectively avoid an uncertainty in the star-formation model. The remaining weak dependences of C_* would vanish when we adopt even a higher threshold density for star formation together with higher resolution.

When we tune the value of C_* in low-$n_{\rm th}$ models, we can obtain similar global star formation properties in the disk galaxies regardless of whether we resolve the detailed structure of the ISM or not. This finding provides support for star-formation models in lower resolution cosmological simulations, which are similar to Run A described in this paper. We will discuss whether it is also true for starburst galaxies in forthcoming papers.

We thank the anonymous referee for his/her fruitful comments and suggestions. The author (TRS) thanks Nozomu Kawakatu and Junichi Baba for helpful discussions. Numerical computations were carried out on the GRAPE system (project ID: g06a15/g07a19) at the Center for Computational Astrophysics, CfCA, of the National Astronomical Observatory of Japan. This project is supported by Grant-in-Aids for Scientific Research (17340059) of JSPS and Molecular-Based New Computational Science Program of National Institutes of Natural Sciences.

References

Abadi, M. G., Navarro, J. F., Steinmetz, M., & Eke, V. R. 2003, ApJ, 591, 499
Bate, M. R., Bonnell, I. A., & Bromm, V. 2003, MNRAS, 339, 577
Bate, M. R., & Burkert, A. 1997, MNRAS, 288, 1060
Broeils, A. H., & Rhee, M.-H. 1997, A&A, 324, 877
Burton, W. B., & Liszt, H. S. 1983, A&AS, 52, 63
Dame, T. M., Hartmann, D., & Thaddeus, P. 2001, ApJ, 547, 792
de Avillez, M. A. 2000a, Ap&SS, 272, 23
de Avillez, M. A. 2000b, MNRAS, 315, 479
de Avillez, M. A., & Berry, D. L. 2001, MNRAS, 328, 708
de Avillez, M. A., & Breitschwerdt, D. 2004, A&A, 425, 899
de Avillez, M. A., & Mac Low, M.-M. 2002, ApJ, 581, 1047
Gingold, R. A., & Monaghan, J. J. 1977, MNRAS, 181, 375
Governato, F., Willman, B., Mayer, L., Brooks, A., Stinson, G., Valenzuela, O., Wadsley, J., & Quinn, T. 2007, MNRAS, 374, 1479
Hartmann, D., & Burton, W. B. 1997, Atlas of Galactic Neutral Hydrogen (Cambridge: Cambridge University Press)
Hubber, D. A., Goodwin, S. P., & Whitworth, A. P. 2006, A&A, 450, 881
James, P. A., et al. 2004, A&A, 414, 23
Janes, K. A., & Phelps, R. L. 1994, AJ, 108, 1773
Katz, N. 1992, ApJ, 391, 502
Katz, N., Weinberg, D. H., & Hernquist, L. 1996, ApJS, 105, 19
Kawata, D., & Gibson, B. K. 2003, MNRAS, 340, 908
Kennicutt, R. C., Jr. 1998, ApJ, 498, 541
Kerr, F. J., Bowers, P. F., Jackson, P. D., & Kerr, M. 1986, A&AS, 66, 373
Klypin, A., Zhao, H. S., & Somerville, R. S. 2002, ApJ, 573, 597
Kravtsov, A. V. 2003, ApJ, 590, L1
Krumholz, M. R., & Tan, J. C. 2007, ApJ, 654, 304
Lada, C. J., & Lada, E. A. 2003, ARA&A, 41, 57
Lucy, L. B. 1977, AJ, 82, 1013
Makino, J. 2004, PASJ, 56, 521
Martin, C. L., & Kennicutt, R. C., Jr. 2001, ApJ, 555, 301
McKee, C. F., & Ostriker, J. P. 1977, ApJ, 218, 148
McKee, C. F., & Williams, J. P. 1997, ApJ, 476, 144
Mihos, J. C., & Hernquist, L. 1994, ApJ, 437, 611
Miyamoto, M., & Nagai, R. 1975, PASJ, 27, 533
Monaghan, J. J. 1992, ARA&A, 30, 543
Monaghan, J. J., & Lattanzio, J. C. 1985, A&A, 149, 135
Myers, P. C. 1978, ApJ, 225, 380
Nakanishi, H., & Sofue, Y. 2003, PASJ, 55, 191
Nakanishi, H., & Sofue, Y. 2006, PASJ, 58, 847
Navarro, J. F., Frenk, C. S., & White, S. D. M. 1997, ApJ, 490, 493
Navarro, J. F., & Steinmetz, M. 2000, ApJ, 538, 477
Navarro, J. F., & White, S. D. M. 1993, MNRAS, 265, 271
Okamoto, T., Eke, V. R., Frenk, C. S., & Jenkins, A. 2005, MNRAS, 363, 1299
Okamoto, T., Jenkins, A., Eke, V. R., Quilis, V., & Frenk, C. S. 2003, MNRAS, 345, 429
Okamoto, T., Nemmen, R. S., & Bower, R. G. 2008, MNRAS, 385, 161
Robertson, B., Yoshida, N., Springel, V., & Hernquist, L. 2004, ApJ, 606, 32
Robertson, B. E., & Kravtsov, A. V. 2008, ApJ, 676, L21
Rosen, A., & Bregman, J. N. 1995, ApJ, 440, 634
Saitoh, T. R., Koda, J., Okamoto, T., Wada, K., & Habe, A. 2006, ApJ, 640, 22
Saitoh, T. R., & Wada, K. 2004, ApJ, 615, L93
Salpeter, E. E. 1955, ApJ, 121, 161
Scalo, J., Vázquez-Semadeni, E., Chappell, D., & Passot, T. 1998, ApJ, 504, 835
Schaye, J., & Dalla Vecchia, C. 2008, MNRAS, 383, 1210
Slyz, A. D., Devriendt, J. E. G., Bryan, G., & Silk, J. 2005, MNRAS, 356, 737
Sommer-Larsen, J., Götz, M., & Portinari, L. 2003, ApJ, 596, 47
Spaans, M., & Norman, C. A. 1997, ApJ, 483, 87
Spergel, D. N., et al. 2003, ApJS, 148, 175
Spitzer, L., Jr. 1978, Physical processes in the interstellar medium (New York: Wiley-Interscience)

Springel, V., & Hernquist, L. 2003, MNRAS, 339, 289
Steinmetz, M., & Müller, E. 1994, A&A, 281, L97
Stinson, G., Seth, A., Katz, N., Wadsley, J., Governato, F., & Quinn, T. 2006, MNRAS, 373, 1074
Tasker, E. J., & Bryan, G. L. 2006, ApJ, 641, 878
Tasker, E. J., & Bryan, G. L. 2008, ApJ, 673, 810
Thacker, R. J., & Couchman, H. M. P. 2001, ApJ, 555, L17
Vázquez-Semadeni, E. 1994, ApJ, 423, 681
Vázquez-Semadeni, E., Gazol, A., & Scalo, J. 2000, ApJ, 540, 271
Wada, K. 2001, ApJ, 559, L41
Wada, K., & Norman, C. A. 1999, ApJ, 516, L13
Wada, K., & Norman, C. A. 2001, ApJ, 547, 172
Wada, K., & Norman, C. A. 2007, ApJ, 660, 276
Wada, K., & Tomisaka, K. 2005, ApJ, 619, 93
Wolfire, M. G., Hollenbach, D., McKee, C. F., Tielens, A. G. G. M., & Bakes, E. L. O. 1995, ApJ, 443, 152
Yepes, G., Kates, R., Khokhlov, A., & Klypin, A. 1997, MNRAS, 284, 235
Zuckerman, B., & Evans, N. J., II. 1974, ApJ, 192, L149